OPEN ACCESS
IOP Publishing
Nanotechnology

Nanotechnology **36** (2025) 065703 (11pp)
https://doi.org/10.1088/1361-6528/ad933a

# Thermal expansion of boron nitride nanotubes and additively manufactured ceramic nanocomposites

**Dingli Wang[1], Rachel Chen[1], Nasim Anjum[1] and Changhong Ke[1,2,*]**

[1] Department of Mechanical Engineering, State University of New York at Binghamton, Binghamton, NY 13902, United States of America
[2] Materials Science and Engineering Program, State University of New York at Binghamton, Binghamton, NY 13902, United States of America

E-mail: cke@binghamton.edu

Received 17 September 2024, revised 3 November 2024
Accepted for publication 15 November 2024
Published 28 November 2024

**Abstract**

Controlling the thermal expansion of ceramic materials is important for many of their applications that involve high-temperature processing and/or working conditions. In this study, we investigate the thermal expansion properties of additively manufactured alumina that is reinforced with boron nitride nanotubes (BNNTs) over a broad temperature range, from room temperature to 900 °C. The coefficient of thermal expansion (CTE) of the BNNT-alumina nanocomposite increases with temperature but decreases with an increase in BNNT loading. The introduction of 0.6% BNNTs results in an approximate 16% reduction in the CTE of alumina. The observed significant CTE reduction of ceramics is attributed to the BNNT's low CTE and ultrahigh Young's modulus, and effective interfacial load transfer at the BNNT-ceramic interface. Micromechanical analysis, based on *in situ* Raman measurements, reveals the transition of thermal-expansion-induced interface straining of nanotubes, which shifts from compression to tension inside the ceramic matrix under thermal loadings. This study provides valuable insights into the thermomechanical behavior of BNNT-reinforced ceramic nanocomposites and contributes to the optimal design of ceramic materials with tunable and zero CTE.

Keywords: ceramics, boron nitride nanotubes, thermal expansion, interfacial load transfer, Raman

## 1. Introduction

Ceramics, like most other engineering materials, expand in response to an increase in temperature. In their applications that involve high-temperature processing and/or working conditions, such as power electronics [1] and aircraft engines [2], differential thermal expansion can lead to residual stress in devices/materials, which ultimately affects their reliability. Therefore, it is desirable to develop ceramic materials with tunable and ideally zero thermal expansion properties that are attractive for a number of demanding applications, such as optical components [3] and aerospace structures. One potential solution is the introduction of nanofillers with suitable thermomechanical properties. Among the reinforcement fillers for ceramics, boron nitride nanotubes (BNNTs) are particularly promising to reduce the thermal expansion of

* Author to whom any correspondence should be addressed.

Original content from this work may be used under the terms of the Creative Commons Attribution 4.0 licence. Any further distribution of this work must maintain attribution to the author(s) and the title of the work, journal citation and DOI.


© 2024 The Author(s). Published by IOP Publishing Ltd

ceramic materials [4] due to their low or even negative coefficient of thermal expansion (CTE) [5] and ultrahigh stiffness. BNNTs [6, 7] are a type of one-dimensional tubular nanostructure with extraordinary structural and mechanical properties and thermal stability [8, 9], which make them effective reinforcements for ceramic materials [10–12]. Because a material's CTE correlates inversely with its Young's modulus [13], BNNT's low CTE properties are commensurate with its ultrahigh Young's modulus of up to 1.3 TPa [14–22]. From an atomistic viewpoint, the CTE of BNNTs comes from the thermal expansion of the B–N bond and dynamic thermal vibration, the latter of which results in bond angular rotation and thermal contraction of the nanotube's apparent axial length [5]. BNNTs are capable of surviving up to 900 °C in air [23] and over 1800 °C in an inert gas environment [24]. These superior thermal and chemical stabilities enable BNNTs to survive the harsh high-temperature manufacturing and/or working conditions that are common for ceramics and compare favorably to their pure carbon counterparts, carbon nanotubes (CNTs), as ceramic fillers. This is because CNTs possess much inferior thermal stability compared to BNNTs and start to oxidize at about 400 °C in air [23], which significantly dwindles the reinforcing potential of the strongest known material as ceramic fillers.

Like mechanical reinforcement, the interfacial load transfer at the nanotube-matrix interface is critical to achieving the envisioned CTE reduction and BNNTs excel in multiple ways. *First*, even though BNNTs are axially rigid, they are supple in the transverse direction [25–28], and thus can conform well to ceramic particle surfaces. The resulting intimate BNNT-ceramic surface is beneficial for an effective interfacial load transfer. *Second*, the covalent and partially ionic nature of the B–N bond leads to a rugged anisotropic energy landscape at the BNNT-ceramic interface [29, 30]. The resulting high energy barrier helps resist shear forces and transfer loads across the interface. The strong BNNT-ceramic interface enables the BNNT filler to effectively constrain crack propagation in ceramics, which increases the fracture strength. The energy dissipation via interfacial frictional slippage due to nanotube pullout from the ceramic matrix helps increase the fracture toughness. Meanwhile, the strong interfacial binding enables BNNT additives to effectively constrain the thermal expansion of the surrounding ceramic matrix due to their much higher Young's modulus and lower CTE than those of ceramics.

To date, research on the use of BNNTs as fillers in ceramic composites has primarily focused on mechanical reinforcement, and substantial improvement in mechanical properties, particularly fracture toughness, has been documented in the literature. For example, Du *et al* reported increases of 131% in fracture strength and 109% in fracture toughness with the addition of 5 wt.% BNNTs in silica ($SiO_2$) [10]. The introduction of 1 wt.% BNNTs in alumina ($Al_2O_3$) [31] and zirconia ($ZrO_2$) [32] reportedly increases their toughness by 35% and 65%, respectively. Recent studies on BNNT-silica composites demonstrate that even the addition of a tiny amount of BNNTs (0.1 wt.%) results in substantial property enhancements, which include ∼72% increase in bending modulus [12], ∼51%–55% increase in flexural strength [11, 12], and ∼46% increase in fracture toughness [11]. Despite these advances, the thermal-mechanical properties, such as the CTE of BNNT-ceramic nanocomposites, remain elusive. Specifically, the CTE of BNNTs has been mostly studied computationally, while experimental measurements remain unexplored. For example, a prior molecular dynamics study reported the CTE of BNNTs ranges from $-0.5 \times 10^{-6}$ to $2 \times 10^{-6}$ °C$^{-1}$ in the longitudinal direction, which depends on factors such as nanotube chirality, diameter, and temperature [5]. It is worth mentioning that single-walled CNTs reportedly exhibit negative CTE properties [33]. However, they are more useful as a filler material under low-temperature processing and working conditions, which are typical for polymer nanocomposites.

This study aims to fill these knowledge gaps by studying the thermal expansion properties of additively manufactured (AM) BNNT-reinforced alumina composites. Alumina is chosen as the matrix material here due to its exceptional properties, including high thermal stability, chemical inertness, and mechanical strength [34–38], and its use in a wide range of applications, such as catalysis supports, filtration membranes, and thermal insulation materials [39–42]. The advent of additive manufacturing techniques, such as digital light processing (DLP), has transformed the manufacturability of ceramic materials [43, 44]. Through its digital, mask-image-projection-based stereolithography process, DLP offers superior manufacturing resolution by selectively curing a photosensitive resin that is mixed with ceramic particles, which allows the creation of intricate internal features and complex geometries that were previously unattainable using conventional ceramic manufacturing techniques (e.g. casting, molding and processing). The DLP-produced AM ceramics possess distinct microstructures (e.g. controllable porosity from the adoption of polymer binders) [45] from those manufactured using conventional methods, which reportedly have significant impacts on their mechanical properties [46]. Because thermal expansion is a type of isotropic deformations, the thermal expansion of the matrix and nanotubes will be better accommodated by the microporous structure, which facilitates the dynamic thermal vibration of BNNTs that results in their negative CTE properties. The study reveals a significant reduction of alumina's CTE by introducing a small amount of BNNTs and the role of the interfacial load transfer in the observed CTE reduction. The findings reported here are useful for better understanding of the thermo-mechanical behavior of BNNT-reinforced ceramic nanocomposites and the optimal design of tunable and zero-CTE materials.

## 2. Materials and methods

### 2.1. Sample preparation

The employed BNNTs (BNNT Materials, LLC.) were produced using high temperature pressure (HTP) techniques [47] with a BN purity of over 99% and a BNNT purity of ∼88% [11]. HTP-BNNTs are reportedly highly crystalline, have very

few walls and small diameters, and are up to a few hundred microns long [47]. Prior studies have shown that HTP-BNNTs have an average diameter of about 2.9 nm, with a dominant double-walled tubular nanostructure [27, 48]. The as-received BNNTs, in the form of puffballs, were dispersed in acetone using ultrasonication bath (155 W, 42 kHz) for about one hour. $\alpha$-Alumina powder (US Research Nanomaterials, Inc) with an average particle size (d50) of about 500 nm and a specific surface area of approximately 20 $m^2$ $g^{-1}$ was used. Two photosensitive resins were employed: HDDA (1,6-hexanediol diacrylate, Thermo Fisher Scientific) and PEGDA (polyethylene glycol diacrylate, Sigma Aldrich) in a mass ratio of 4:1. A surfactant (BYK-111, BYK Additives & Instruments) was utilized to facilitate the dispersion of ceramic powders into the resin system. TPO (diphenyl (2,4,6-trimethylbenzoyl) phosphine oxide, Sigma Aldrich) was used as the photoinitiator to crosslink the resins.

To manufacture BNNT-alumina nanocomposite specimens, alumina powders were first added to the BNNT/acetone suspension, and the mixture was processed in a tip sonicator (Branson Digital Sonifier 450, 20 kHz, 400 W) for 10 min to achieve uniform dispersion. The resulting alumina/BNNT/acetone suspension was then thermally baked at 90 °C to remove the solvent. The dried ceramic/BNNT chunk was ground using a mortar and then passed through a 50-mesh sieve to obtain uniformly sized alumina nanocomposite powder. The composite powder was then incorporated into the HDDA-PEGDA resin system, which was followed by the addition of BYK-111 (2.5 wt.% relative to solid loading) and TPO (1 wt.% relative to liquid loading). Finally, a uniform ceramic composite slurry was obtained using a shearing mixer (FlackTek Inc.) at 3000 rpm for one hour.

The green body of the alumina composite was manufactured using a 'bottom up' DLP 3D printer (Hunter, Flashforge Inc.) that utilizes a 405 nm irradiation source. A transparent fluorinated ethylene propylene sheet was affixed to the bottom of the vat to reduce the release force of each layer. Each layer was set to a thickness of 50 $\mu$m [49, 50] with an exposure time of three seconds. After the layer-by-layer fabrication, green bodies were thermally processed to remove the polymer binders in three consecutive steps: (1) heating from room temperature (about 20 °C) to 403 °C at a rate of 0.5 °C $min^{-1}$ and then holding for 30 min; (2) heating from 403 °C to 515 °C at a rate of 0.5 °C $min^{-1}$ and then holding for 30 min; (3) heating from 515 °C to 750 °C at a rate of 1 °C $min^{-1}$, holding for one hour, and then naturally cooling down. The debonded BNNT-alumina specimen was sintered under the following conditions: (1) heating from room temperature to 1000 °C at a rate of 4 °C $min^{-1}$; (2) heating from 1000 °C to 1450 °C at a rate of 2 °C $min^{-1}$, holding for one hour at 1450 °C, and then naturally cooling down. The alumina composites with various BNNT loadings of 0.0%, 0.2%, 0.4%, and 0.6% were fabricated using the above manufacturing process. Unless explicitly indicated, BNNT concentrations mentioned throughout this study are expressed as weight percentages.

### 2.2. Characterization

Thermogravimetric analysis (TGA) was conducted at a heating rate of 10 °C $min^{-1}$ in an ambient environment to investigate the debinding weight loss kinetics of the DLP-printed alumina green body using a TA Instruments Q50 analyzer. For phase analysis, x-ray diffraction (XRD) was performed on a PANalytical X'Pert PRO diffractometer equipped with a sealed Cu tube for Cu K$\alpha$ radiation ($\lambda \approx 1.54$ Å) at 45 kV and 40 mA, scanning over a $2\theta$ range of 10°–70°. The density of the BNNT-alumina specimen was determined by dividing the mass by the volume, while the porosity was calculated based on the theoretical density of alumina (3.9 g $cm^{-3}$) [51]. Thermomechanical analysis (TMA) and thermal expansion measurements were conducted using a TMA Q400 (TA Instruments) from room temperature to 900 °C at a heating rate of 10 °C $min^{-1}$ in a helium atmosphere. The microstructure and morphology of the DLP-produced alumina nanocomposite were examined using a Zeiss Supra 55 scanning electron microscope (SEM). Raman spectroscopy was performed using a Renishaw inVia Raman system equipped with a 532 nm excitation laser, a grating of 2400 lines/mm, and a 50× objective lens.

## 3. Results and discussion

### 3.1. Thermal expansion and CTE measurements

Figure 1(a) shows the as-printed green body and the as-sintered parts of the BNNT-alumina nanocomposite. The volume shrinkage values for alumina with BNNT concentrations of 0.0%, 0.2%, 0.4%, and 0.6% were calculated to be approximately 28%, 26%, 24%, and 22%, respectively. Figure 1(b) presents the TGA results of the printed green body. The derivative thermogravimetric (DTG) analysis reveals two significant peaks at approximately 403 °C and 515 °C. These temperatures were selected as holding points to minimize crack formation during the thermal debinding process. At around 600 °C, the weight of the green body stabilizes, which indicates the complete removal of binders. Figure 1(c) shows the respective XRD patterns for raw alumina powders, as-sintered monolithic alumina, and as-sintered 0.6% BNNT-alumina. In all cases, only the $\alpha$-alumina phase was detected, which indicates that the addition of BNNT does not affect its phase composition. This stability in phase composition suggests that BNNT incorporation does not alter the crystalline structure of the alumina matrix, which is advantageous for the preservation of the inherent properties of alumina. Figure 1(d) shows the density and porosity of the sintered BNNT-alumina with varying nanotube loadings. The addition of a small amount of BNNTs (0.2% to 0.6%) to $\alpha$-alumina results in a noticeable decrease in density and an increase in porosity. For example, the introduction of 0.6% BNNT decreases the density of alumina by about 13%, from 2.3 g $cm^{-3}$ to 2.0 g $cm^{-3}$, which is accompanied by a similar percentage increase in porosity, from 42.1% to 48.5%. The observed density/porosity

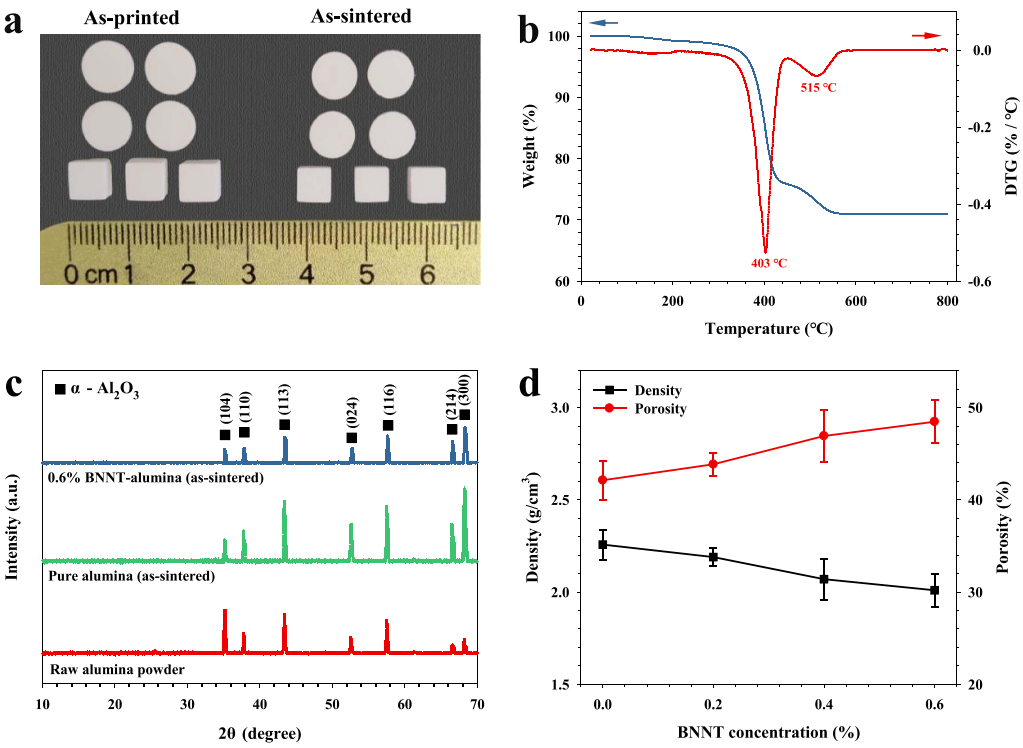


**Figure 1.** Structural and material characterization of 3D-printed BNNT-alumina nanocomposites. (a) Optical images of as-printed and as-sintered composite specimens (0.6% BNNT); (b) TGA and DTG graphs of as-printed composite specimens; (c) XRD characterization of raw alumina powder, sintered monolithic alumina, and sintered 0.6% BNNT-alumina; (d) density and porosity of BNNT-alumina.

changes can be attributed to the following factors: (1) BNNT possesses a lower density (∼1.35 g $cm^{-3}$) [52] than that of DLP-printed alumina (∼2.3 g $cm^{-3}$); (2) Due to the polymer debinding, the density of AM-produced pure alumina (∼2.3 g $cm^{-3}$) is substantially lower than that of monolithic alumina (3.9 g $cm^{-3}$) [51]. BNNT has a much lower CTE than alumina (∼$8 \times 10^{-6}$ °$C^{-1}$) [53]. The addition of BNNTs reduces the overall CTE of the alumina powder, which subsequently decreases the sintering driving force and lowers the density of the AM-produced BNNT-alumina; (3) BNNTs are likely to be present between the alumina particles, hindering their densification during the sintering process. These factors collectively lead to the observed decrease in the macroscopic density of BNNT-alumina relative to pure alumina.

Figure 2(a) shows the thermal expansion strain curves of BNNT-alumina. The thermal expansion strain here is calculated as $\frac{\Delta l}{l}$, where $l$ is the original length and $\Delta l$ is the length change. As expected, the thermal expansion increases with temperature, but the rate of increase diminishes with higher BNNT concentration. For instance, at 900 °C, the thermal expansion strain of BNNT-alumina is found to be 0.66% for 0.2% BNNT, 0.64% for 0.4% BNNT, and 0.61% for 0.6% BNNT, compared to 0.71% for pure alumina.

Figure 2(b) shows the evolution of CTE with temperatures for BNNT-alumina. The CTE is calculated as.$\alpha = \frac{\mathrm{d}l}{l \cdot \mathrm{d}T} = \frac{\mathrm{d}(\ln l)}{\mathrm{d}T}$ The thermal expansion curves shown in figure 2(a) can be perfectly curve-fitted using quadratic functions, with a coefficient of determination ($R$-squared) of approximately 1.0. Therefore, as exhibited in figure 2(b), the CTE of BNNT-alumina shows a linear relationship with temperature. The measured CTE of pure alumina at room temperature is about $6.90 \times 10^{-6}$ °$C^{-1}$ or 6.90 ppm °$C^{-1}$, which increases to 9.40 ppm °$C^{-1}$ at 900 °C. In comparison, the CTE of BNNT-alumina with 0.2%, 0.4% and 0.6% BNNTs at room temperature (900 °C) is found to be 6.31 (8.88), 5.96 (8.51), and 5.81 (7.91) ppm °$C^{-1}$, respectively. Consistently, the CTE of alumina decreases with an increase in BNNT loading. The observed CTE reduction is independent of temperature and reaches about 16% under a BNNT loading of 0.6%.

We employ a modified Turner's model to quantify the CTE of BNNTs based on the thermal expansion measurements of BNNT-alumina. The CTE of the nanotube composite is given as [54, 55]:

$$\alpha_c(t) = \frac{\alpha_{\mathrm{m}}(1 - V_{\mathrm{nt}}) E_{\mathrm{m}}(t) + \eta \alpha_{\mathrm{nt}} V_{\mathrm{nt}} E_{\mathrm{nt}}(t)}{(1 - V_{\mathrm{nt}}) E_{\mathrm{m}}(t) + \eta V_{\mathrm{nt}} E_{\mathrm{nt}}(t)} \quad (1)$$

where $E_{\mathrm{m}}(t)$ and $E_{\mathrm{nt}}(t)$ represent the Young's moduli of the matrix and nanotubes, respectively, and both decrease with an increase in temperature [56, 57]: $E_{\mathrm{m}}(t) = E_{\mathrm{m}}^{\mathrm{RT}}\left(1 - \frac{t-20}{8800}\right)$ and $E_{\mathrm{nt}}(t) = E_{\mathrm{nt}}^{\mathrm{RT}}\left(1 - \frac{t-20}{8800}\right)$, where $E_{\mathrm{m}}^{\mathrm{RT}} = 33.1$ GPa is the elastic modulus of DLP-printed alumina at room temperature that was measured using three-point bending tests (see figure S1 in the *supplemental information*) and $E_{\mathrm{nt}}^{\mathrm{RT}} = 1.07$ GPa is the elastic modulus of BNNTs at room temperature [20]. $\alpha_{\mathrm{m}}$ and $\alpha_{\mathrm{nt}}$ denote the CTEs of the matrix and the nanotube, respectively.

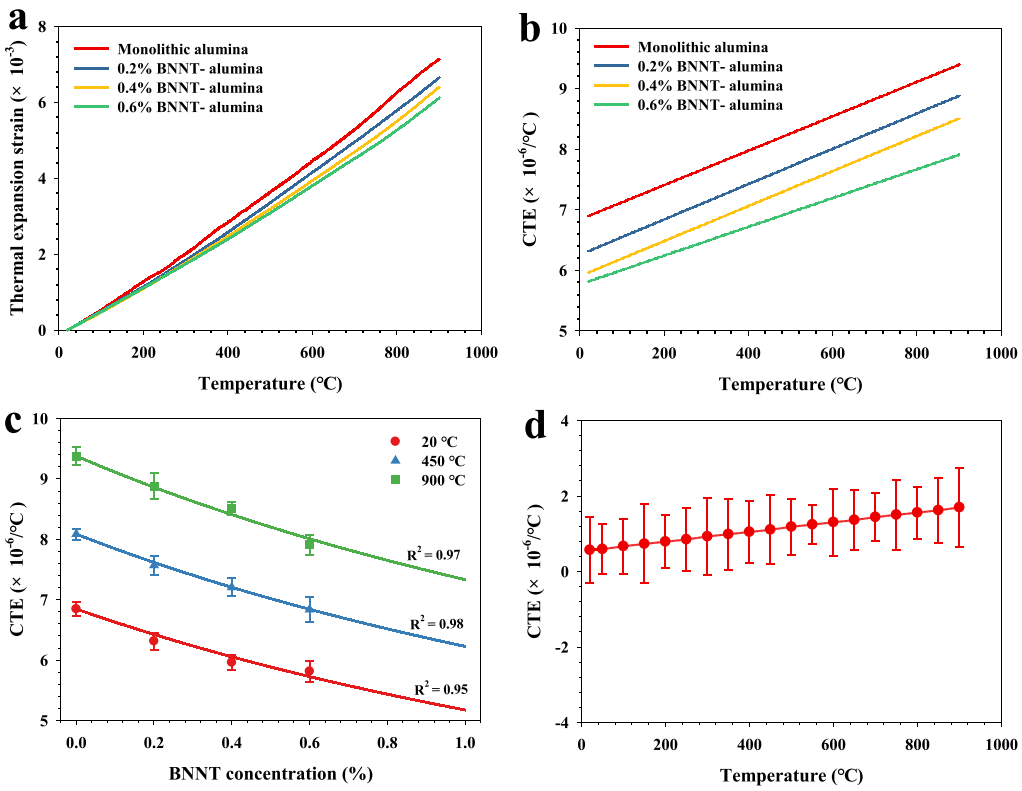


**Figure 2.** Thermal expansion measurements of BNNT-alumina nanocomposites: (a) thermal expansion strain; (b) CTE; (c) fitted CTE curves using a modified Turner's model at selected temperatures; (d) CTE of BNNTs.

$V_{nt}$ is the volume fraction of the nanotube. $\eta$ is a parameter that accounts for the orientation of the nanotubes inside the matrix ($\eta = 1$ for perfectly aligned nanotubes). Here, the nanotubes inside the ceramic matrix are considered to have a fully random orientation, which is confirmed by polarized Raman measurements (see figure S2). For randomly oriented nanotubes, $\eta = (1-\nu_m)/2$, where $\nu_m$ is the Poisson's ratio of the matrix ($\nu_m = 0.23$ for alumina) [11]. Figure 2(c) shows the fitted curves derived from the modified Turner's model, based on experimentally determined CTEs of BNNT-alumina at three selected temperatures (i.e. 20 °C, 450 °C, and 900 °C). The volume fractions of BNNTs, $V_{nt}$, is calculated to be 0.58%, 1.15%, and 1.71% for BNNT loadings of 0.2%, 0.4%, and 0.6%, respectively, which are assumed as constants (i.e. independent of temperature). The effective CTE of BNNTs is found to be about 0.57 ppm °C$^{-1}$ (20 °C), 1.11 ppm °C$^{-1}$ (450 °C), and 1.70 ppm °C$^{-1}$ (900 °C) with a curve-fitting *R*-squared value of 0.95–0.98. Figure 2(d) shows the CTE of BNNTs across the entire temperature range, which displays an increasing trend with temperature. The calculated CTE of BNNTs, along with the experimentally measured CTE values for alumina and its BNNT nanocomposites, is listed in table 1. The results of CTE of BNNTs are consistent with prior computational results based on MD simulations [5]. Specifically, our measured CTE of BNNTs of 2.9 nm in median diameter at room temperature (∼0.57 ppm °C$^{-1}$) is close to the MD simulated value (∼0.4 ppm °C$^{-1}$) for BNNTs of a diameter of 2.8 nm. Furthermore, our experimental results show the CTE of BNNTs increases by 84.2% (from ∼0.57 ppm °C$^{-1}$ to ∼1.05 ppm °C$^{-1}$) when the temperature increases from 20 °C to 400 °C, which is in close agreement with the simulation results (82.5% increase in CTE, from ∼0.4 ppm °C$^{-1}$ to ∼0.73 ppm °C$^{-1}$).

### 3.2. *Structural morphology analysis of BNNT-alumina*

Figure 3(a) shows the fracture surface morphology of 0.6% BNNT-alumina, which reveals nanotubes that distinctly protrude from and are embedded within the alumina matrix. A sintering neck, highlighted by the dashed box, is observed despite the presence of numerous pores after sintering. Figure 3(b) shows BNNTs bridging a microcrack with an approximate 2 $\mu$m opening length. The BNNTs are uniformly dispersed within the alumina matrix, in which no significant agglomeration is observed. This uniform dispersion facilitates both reinforcement and the CTE reduction effect. Notably, these nanotubes bridge neighboring alumina particles, which facilitates effective load transfer between the ceramic matrix and nanotubes under thermal loading conditions. These phenomena help explain why the CTE of BNNT-alumina is noticeably lower than that of pure alumina. Figures 3(c)–(f) present the SEM-EDX mapping results for 0.6% BNNT-alumina. The elemental distribution analysis reveals a uniform presence of aluminum, oxygen, boron, and nitrogen atoms across the examined surface. This homogeneous distribution further demonstrates the uniform dispersion of BNNTs within the

**Table 1.** Summary of CTE of BNNTs, alumina, and BNNT-alumina composites.

| | Coefficient of thermal expansion (ppm $^{\circ}C^{-1}$) | | | | |
|---|---|---|---|---|---|
| Temperature ($^{\circ}C$) | BNNT | Alumina | 0.2% BNNT-alumina | 0.4% BNNT-alumina | 0.6% BNNT-alumina |
| 20 | 0.57 ± 0.88 | 6.90 ± 0.42 | 6.31 ± 0.29 | 5.96 ± 0.20 | 5.81 ± 0.50 |
| 50 | 0.59 ± 0.67 | 6.98 ± 0.23 | 6.40 ± 0.23 | 6.05 ± 0.31 | 5.89 ± 0.42 |
| 100 | 0.67 ± 0.72 | 7.12 ± 0.21 | 6.55 ± 0.26 | 6.19 ± 0.39 | 6.00 ± 0.29 |
| 150 | 0.73 ± 1.05 | 7.27 ± 0.45 | 6.69 ± 0.15 | 6.34 ± 0.44 | 6.12 ± 0.47 |
| 200 | 0.79 ± 0.70 | 7.41 ± 0.35 | 6.84 ± 0.21 | 6.48 ± 0.17 | 6.24 ± 0.28 |
| 250 | 0.85 ± 0.84 | 7.52 ± 0.19 | 6.99 ± 0.16 | 6.63 ± 0.48 | 6.36 ± 0.53 |
| 300 | 0.93 ± 1.02 | 7.7 ± 0.48 | 7.13 ± 0.41 | 6.77 ± 0.32 | 6.48 ± 0.14 |
| 350 | 0.99 ± 0.94 | 7.83 ± 0.25 | 7.28 ± 0.39 | 6.92 ± 0.42 | 6.60 ± 0.52 |
| 400 | 1.05 ± 0.82 | 7.89 ± 0.36 | 7.42 ± 0.47 | 7.06 ± 0.11 | 6.72 ± 0.44 |
| 450 | 1.11 ± 0.92 | 8.12 ± 0.34 | 7.57 ± 0.38 | 7.21 ± 0.39 | 6.84 ± 0.24 |
| 500 | 1.18 ± 0.73 | 8.26 ± 0.36 | 7.71 ± 0.44 | 7.35 ± 0.16 | 6.96 ± 0.13 |
| 550 | 1.24 ± 0.51 | 8.40 ± 0.22 | 7.86 ± 0.14 | 7.49 ± 0.11 | 7.07 ± 0.47 |
| 600 | 1.30 ± 0.89 | 8.54 ± 0.42 | 8.00 ± 0.49 | 7.64 ± 0.23 | 7.19 ± 0.11 |
| 650 | 1.36 ± 0.80 | 8.69 ± 0.32 | 8.15 ± 0.38 | 7.78 ± 0.25 | 7.31 ± 0.37 |
| 700 | 1.44 ± 0.64 | 8.83 ± 0.17 | 8.30 ± 0.29 | 7.93 ± 0.33 | 7.43 ± 0.37 |
| 750 | 1.50 ± 0.93 | 8.97 ± 0.44 | 8.44 ± 0.22 | 8.07 ± 0.38 | 7.55 ± 0.33 |
| 800 | 1.56 ± 0.69 | 9.11 ± 0.33 | 8.59 ± 0.14 | 8.22 ± 0.16 | 7.67 ± 0.37 |
| 850 | 1.62 ± 0.86 | 9.25 ± 0.42 | 8.74 ± 0.23 | 8.36 ± 0.29 | 7.79 ± 0.36 |
| 900 | 1.70 ± 1.05 | 9.40 ± 0.44 | 8.88 ± 0.12 | 8.51 ± 0.55 | 7.91 ± 0.22 |

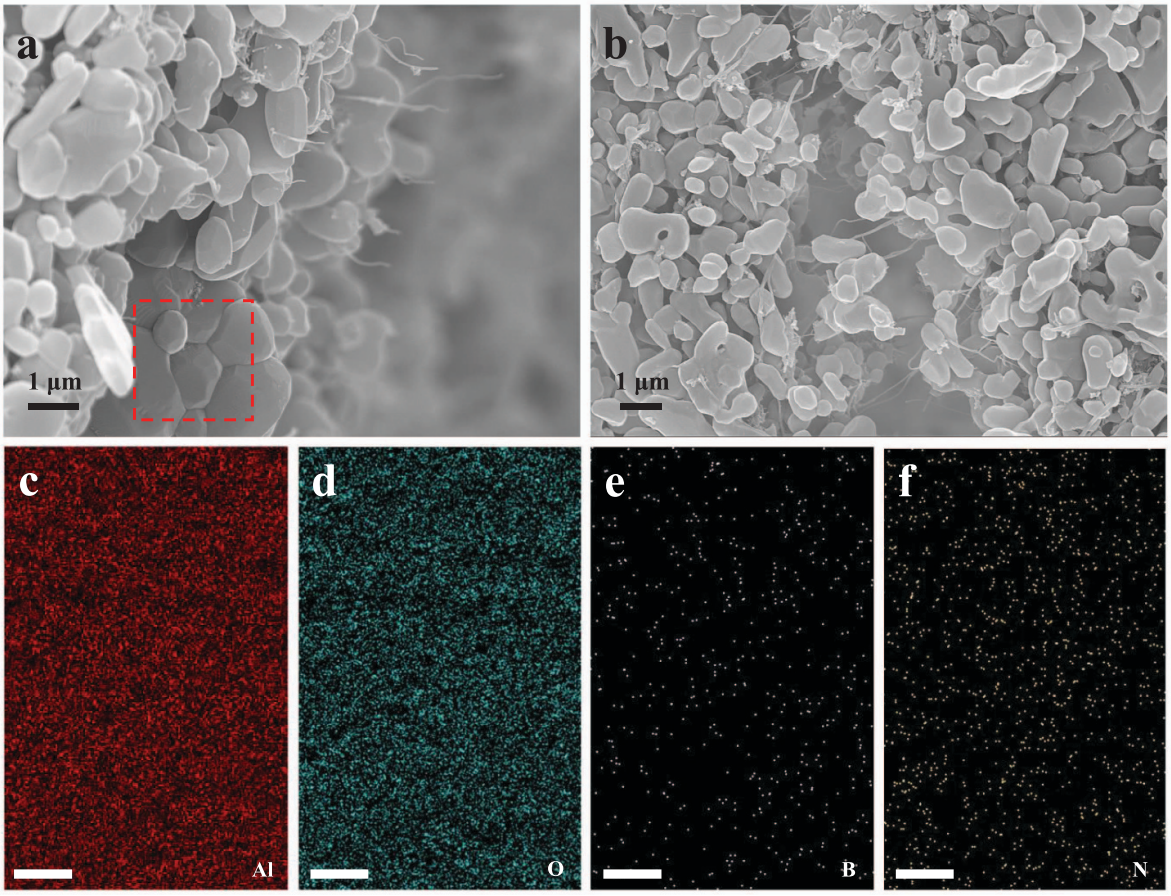


**Figure 3.** Structural morphology of 0.6% BNNT-alumina nanocomposites: (a) SEM image of a typical fracture surface showing protruding nanotubes that were pulled out from the ceramic matrix; (b) SEM image of a microcrack with bridging and protruding BNNTs. (c–f) EDX elemental distribution: (c) aluminum, (d) oxygen, (e) boron, and (f) nitrogen. The scale bars in (c)–(f) are all 20 $\mu$m.

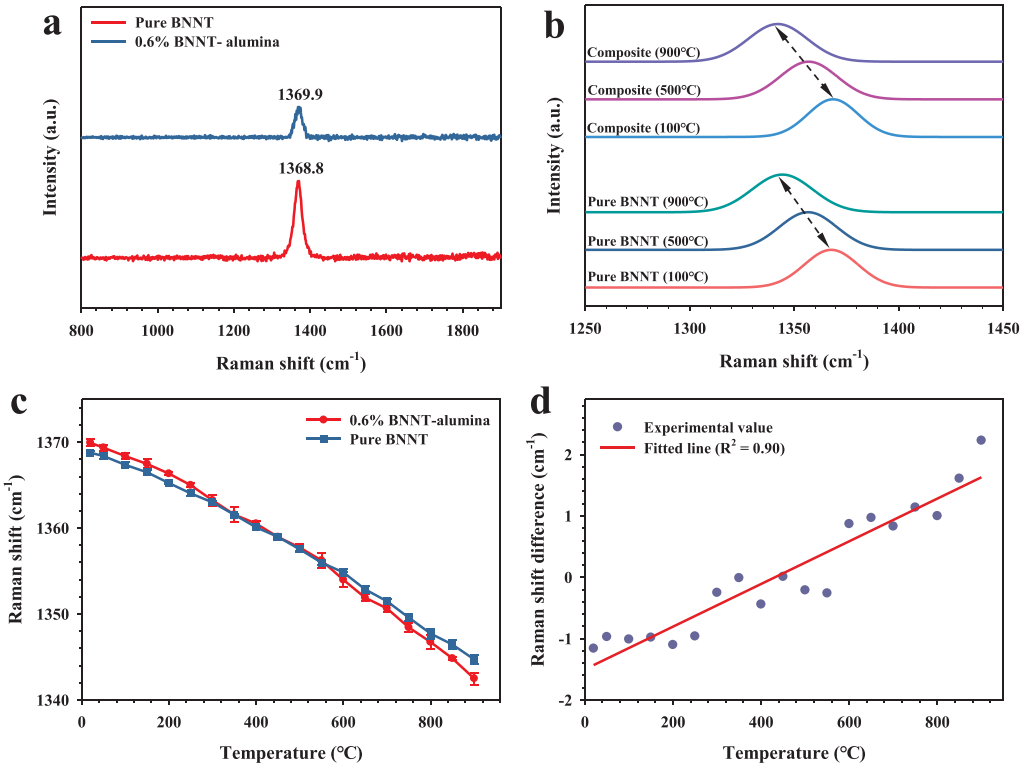


**Figure 4.** *In situ* Raman measurements of pure BNNTs and 0.6% BNNT-alumina nanocomposites. (a) Typical Raman spectra at room temperature; (b) selected Raman spectra from room temperature to 900 °C; (c) Raman G-band peak wavenumber of BNNTs and BNNT-alumina; (d) difference in measured Raman G-band wavenumber between BNNTs and BNNT-alumina.

alumina matrix. The consistent spatial arrangement of all constituent elements suggests an effective integration of the nanotubes into the ceramic structure, which is crucial for optimization of the composite's properties.

### *3.3. In situ Raman measurement and interfacial load transfer analysis*

The Raman spectrum of BNNTs responds to mechanical strain due to the resulting B–N bond length change [58, 59]. Specifically, the Raman wavenumber of the BNNT G-band downshifts under tensile strain (*redshift*) and upshifts under compressive strain (*blueshift*). Figure 4(a) shows typical Raman spectra for pure BNNTs and 0.6% BNNT-alumina, both of which exhibit a BNNT Raman G-band around 1369 $cm^{-1}$. It is noted that the G-band intensity becomes weaker in composites with lower BNNT loadings. To ensure a sufficiently robust G-band signal, Raman characterization was conducted exclusively on 0.6% BNNT-alumina specimens. Notably, the G-band of the nanocomposite displays a blue-shift relative to that of pristine BNNTs, which indicates that nanotubes inside the matrix predominantly experience compressive strain. This compressive strain may arise from two sources: (1) volumetric shrinkage of the nanocomposite green body during sintering, which exerts compressive forces on the nanotube, and (2) the development of residual compressive strain in the nanotube upon cooling from the high-temperature sintering process, due to the CTE mismatch between BNNTs and alumina.

Because the alumina matrix thermally expands more than BNNTs upon heating, shear stress develops at the nanotube-matrix interface. We conducted *in situ* Raman measurements for both pure BNNTs and 0.6% BNNT-alumina from room temperature to 900 °C to investigate the mechanical straining of nanotubes within the ceramic matrix. Circular disk-shaped specimens of BNNT-alumina (figure 1(a)), approximately 6 mm in diameter and 3 mm in thickness, were placed on a computer-controlled heating stage (Linkam TS 1500). The Raman laser spot was carefully positioned in the central region of the sample to minimize edge effects during heating. The sample was incrementally heated from room temperature at a rate of 10 °C per minute and held for 20 min at each 50 °C mark before the Raman recording to ensure a steady-state target temperature inside the sample. Pure BNNTs, in the form of puffballs, were characterized as controls using the same testing parameters.

Figure 4(b) shows representative *in situ* Raman spectra recorded at 100 °C, 500 °C, and 900 °C for both pristine BNNTs and 0.6% BNNT-alumina. The composite exhibits a more pronounced G-band redshift of ∼25.9 $cm^{-1}$ between 100 °C and 900 °C, compared to merely ∼22.6 $cm^{-1}$ for pristine BNNTs over the same temperature range. This discrepancy in Raman redshift magnitude can be attributed to distinct loading conditions: pristine BNNTs experience

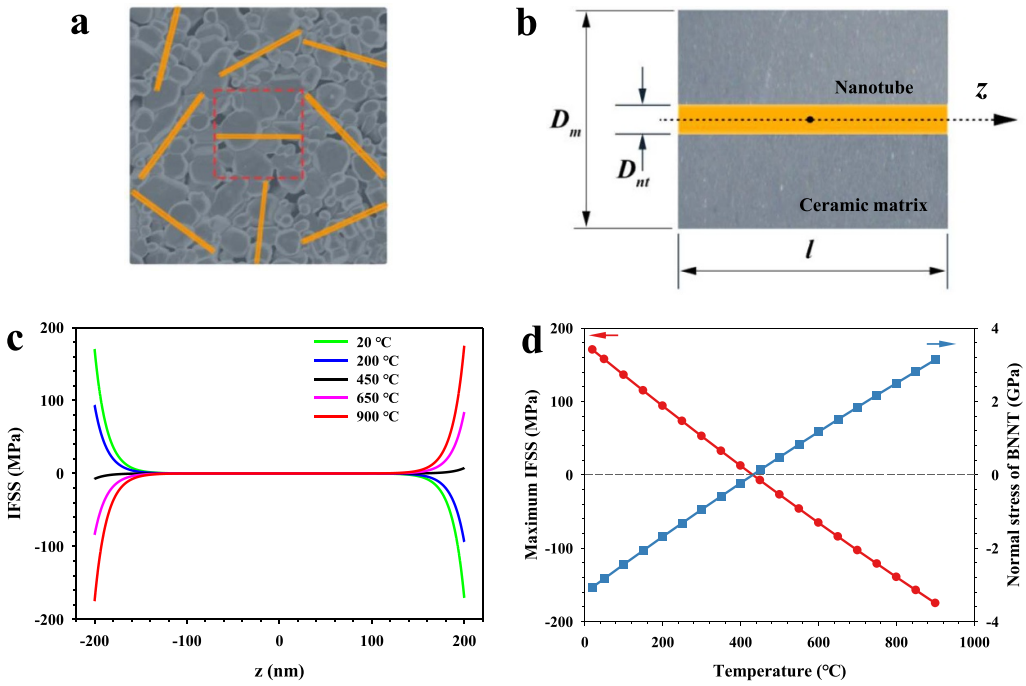


**Figure 5.** Interfacial load transfer characteristics of BNNT-alumina nanocomposites: (a) schematics of the equivalent configuration of the BNNT-alumina; (b) schematic of single-nanotube nanocomposite; (c) selected interfacial shear stress distribution profiles from room temperature to 900 °C; (d) the dependences of the maximum interfacial shear stress at the left end of the nanotube and normal stress inside the nanotube on temperature. The signs indicate the directions of the interfacial shear stress and the normal stress (tensile or compressive).

redshift solely due to thermally induced changes in bond length, whereas BNNTs within the composite are subjected to both thermal effects and mechanical straining induced by the CTE mismatch between BNNTs and the matrix.

Figure 4(c) shows the temperature dependence of the Raman G-band peak wavenumber for both pristine BNNTs and 0.6% BNNT-alumina. Initially, the composite exhibits a higher G-band wavenumber (∼1369.9 $cm^{-1}$) compared to pristine BNNTs (∼1368.8 $cm^{-1}$), which indicates residual compressive strain in the embedded nanotubes. As the temperature approaches ∼450 °C, the G-band wavenumbers of both materials converge, which signifies the full release of the residual compressive strain caused by the CTE mismatch. Upon further heating from 450 °C to 900 °C, the Raman wavenumber of the G-band in BNNT-alumina becomes lower than that of pure BNNTs, and the difference progressively increases with temperature. This indicates the onset and gradual intensification of tensile straining in the embedded BNNT. Figure 4(d) shows the temperature-dependent evolution of the differential Raman G-band wavenumber between BNNT-alumina and pristine BNNTs during *in situ* heating, which displays a linear dependence. The wavenumber difference is found to be approximately −1.43 $cm^{-1}$ at room temperature and 1.63 $cm^{-1}$ at 900 °C. The temperature-induced total shift of 3.06 $cm^{-1}$ in the Raman G-band wavenumber can be attributed to mechanical strain that is calculated to be ∼0.61% based on the CTE mismatch, given by $\varepsilon_{nt} = \int (\alpha_m - \alpha_{nt})\,dt$. The Raman G-band wavenumber shift per percentage of mechanical strain is calculated to be about 4.0 $cm^{-1}$/%, which compares favorably with the values reported for BNNT-polymer composites (1.2–4.2 $cm^{-1}$/%) [52, 59], and is modestly lower than the values reported for BNNT-silica composites (4.7–5.0 $cm^{-1}$/%) [11]. The residual strain of BNNTs in BNNT-alumina at room temperature is calculated to be ∼0.29% based on a Raman wavenumber shift of 1.43 $cm^{-1}$. It is also important to highlight that the *in situ* Raman measurement reveals that the nanotube-matrix interface remains in intimate contact throughout the heating and cooling, with no evidence of interfacial slippage.

Next, we investigate the interfacial shear stress (IFSS) transfer characteristics of BNNT-alumina induced by thermal loading using a shear-lag micromechanics model [11]. The model, as illustrated in figure 5(a), is established under the following two *assumptions*: (1) the BNNTs are uniformly and sparsely dispersed in the alumina matrix with identical composite cell dimensions; (2) the interface between the nanotube and the ceramic matrix is uniform and perfectly bonded. The first assumption considers the low concentration of BNNTs and ignores the inter-nanotube interactions, while the second assumption ignores the inhomogeneity at the nanotube-matrix binding interface. Thus, the IFSS behavior of BNNT-alumina can be represented using a simplified single-nanotube composite configuration (figure 5(b)), which comprises a straight nanotube of diameter $D_{nt}$ and length $l$ inside a same-length cylindrical matrix of diameter $D_m$. The IFSS distribution on the nanotube-matrix interface $\tau$ is given as [60],

$$\tau = \frac{E_{nt}(t)\,\varepsilon_{nt} n}{2} \frac{\cosh(2n \cdot z/D_{nt})}{\sinh(n \cdot l/D_{nt})}, \tag{2}$$

where $z$ is the coordinate along the longitudinal axis of the nanotube, and $n = \sqrt{\frac{E_m(t)}{E_{nt}(t)\cdot(1+\nu_m)\cdot\log\left(\frac{D_m}{D_{nt}}\right)}}$. For 0.6% BNNT-alumina with $D_{nt} = 2.9$ nm, $D_m$ is calculated to be 31.3 nm. The effective IFSS distribution profile is calculated to be independent of the nanotube length ($l$) when $l > 75$ nm, considering an IFSS threshold value of 1 MPa. Assuming a nanotube length $l = 400$ nm, figure 5(c) shows the evolution of the IFSS distribution profiles along the nanotube axis from room temperature to 900 °C. Figure 5(d) shows the evolutions of the maximum IFSS that occurs at the left end ($z = -l/2$) of the nanotube and the maximum normal stress within the nanotube. At room temperature, the residual normal stress inside the BNNT for 0.6% BNNT-alumina is compressive, with a calculated magnitude of approximately 3.1 GPa. This value is based on the measured nanotube strain of approximately 0.29%. As the temperature gradually increases, the residual compressive strain in the nanotube is progressively released and approaches zero when the temperature reaches approximately 450 °C. It is noteworthy that, even though there is zero normal stress in the nanotube at this temperature, effective load transfer to the ceramic matrix still occurs, which contributes to the reduction in the bulk CTE of BNNT-alumina. With a further temperature increase up to 900 °C, the nanotube inside the composite is found to be under tensile straining. At 900 °C, the maximum tensile stress in the nanotube is calculated to be approximately 3.5 GPa, corresponding to a tensile strain of ∼0.33%. This measured tensile stress is significantly below the tensile strength of HTP-BNNT, which is reported to be above 60 GPa at room temperature [61]. The maximum IFSS reaches ∼171 MPa at room temperature and ∼175 MPa at 900 °C. The average IFSS for the entire effective load transfer region is calculated to be ∼27.4 MPa at room temperature and ∼28.1 MPa at 900 °C, which are substantially lower than the average IFSS (∼46 MPa) reported for nearly perfectly bound interfaces between single HTP-BNNTs and the alumina matrix [61]. This analysis further supports that the BNNT-alumina interface remains intact (i.e. no interface slip) during heating up to 900 °C and suggests that it could potentially withstand even higher temperatures in a vacuum or inert gas environment.

### *3.4. CTE reduction in aligned nanotube-reinforced ceramics*

Here, we perform a theoretical analysis to evaluate the ultimate potential of BNNTs to reduce the CTE of ceramics. We investigate the CTE of BNNT-alumina composites with perfectly aligned nanotubes ($\eta = 1$ in equation (1)). Such composites with nearly perfectly aligned nanotubes were recently reported using electrospinning techniques, in which nanotubes were well-aligned along the fiber's longitudinal direction by viscous shear forces [52, 60]. Figure 6 shows the predicted CTE of BNNT-alumina composites with perfectly aligned nanotubes at three selected temperatures (20 °C, 450 °C, and 900 °C). The CTE decreases with increasing BNNT loading at all the selected temperatures. For example, the incorporation of 5% of BNNTs results in an approximately

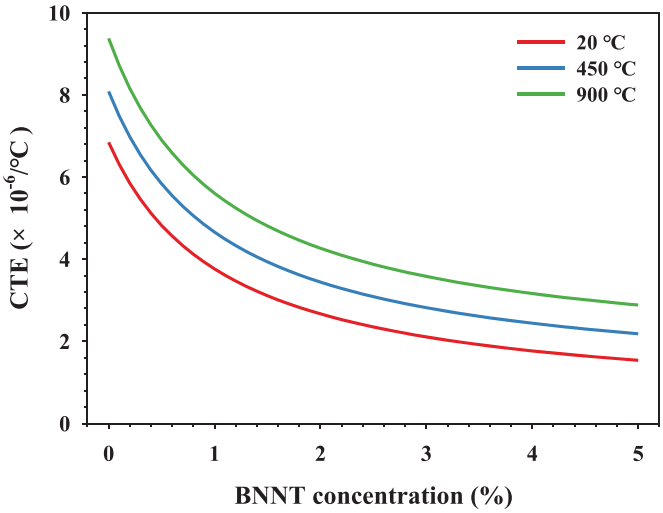


**Figure 6.** Predicted CTE of alumina nanocomposites with perfectly aligned BNNTs at 20 °C, 450 °C and 900 °C.

78% reduction in the CTE of alumina, which decreases from ∼6.8 ppm °C$^{-1}$ to ∼1.5 ppm °C$^{-1}$ at 20 °C. Similar reductions in CTE are observed at 450 °C and 900 °C. This analysis further demonstrates the potential of BNNTs as fillers to substantially decrease the CTE of ceramics and lays the scientific foundation for future studies that aim to optimize the thermomechanical properties of BNNT-ceramic composites by controlling nanotube alignment.

## 4. Conclusions

The thermal expansion properties of BNNT-alumina nanocomposites are investigated. The introduction of small amounts of BNNTs induces a significant CTE reduction of alumina. The reduction is attributed to low CTE and ultrahigh Young's modulus of BNNTs and the effective load transfer at the interface between BNNTs and the ceramic matrix. This study is among the first to report the CTE of BNNTs, which is found to be about 0.57 ppm °C$^{-1}$ at room temperature and increases with temperature. The *in situ* Raman measurement reveals the evolution of the thermally induced interfacial load transfer at the BNNT-matrix interface at up to 900 °C in air and the mechanical straining of BNNTs inside the matrix. The study reveals the superior mechanical and thermal stability of BNNTs and their potential as fillers for tuning the thermal expansion of ceramics. This study provides crucial insights into the thermomechanical behavior of BNNT-reinforced ceramic nanocomposites and contributes to the optimal design of tunable and zero-CTE materials.

## Data availability statement

All data that support the findings of this study are included within the article (and any supplementary files).

## Acknowledgments

The authors acknowledge the support of the National Science Foundation under Grant Nos. CMMI 2009134, 2406763, and 2425706 and the support of the SUNY System Administration under SUNY Research Seed Grant Award #241008. R.C. acknowledges the fellowship support by the New York Space Grant Consortium.

## Conflict of interest

The authors have no conflicts to disclose.

## ORCID iDs

Dingli Wang https://orcid.org/0009-0007-0220-9245
Nasim Anjum https://orcid.org/0000-0003-4715-2071
Changhong Ke https://orcid.org/0000-0002-5170-9859

## References

[1] Hong K, Lee T H, Suh J M, Yoon S-H and Jang H W 2019 Perspectives and challenges in multilayer ceramic capacitors for next generation electronics *J. Mater. Chem.* C **7** 9782–802
[2] Wang X, Gao X, Zhang Z, Cheng L, Ma H and Yang W 2021 Advances in modifications and high-temperature applications of silicon carbide ceramic matrix composites in aerospace: a focused review *J. Eur. Ceram. Soc.* **41** 4671–88
[3] Hartmann P, Jedamzik R, Carré A, Krieg J and Westerhoff T 2021 Glass ceramic ZERODUR®: even closer to zero thermal expansion: a review, part 1 *J. Astron. Telesc. Instrum. Syst.* **7** 020901
[4] Heon Kim C, Go E B and Tae Kim H 2020 Thermophysical properties of zirconia toughened alumina ceramics with boron nitride nanotubes addition *Heat Transfer Eng.* **41** 1354–64
[5] Mashreghi A 2012 Thermal expansion/contraction of boron nitride nanotubes in axial, radial and circumferential directions *Comput. Mater. Sci.* **65** 356–64
[6] Rubio A, Corkill J L and Cohen M L 1994 Theory of graphitic boron-nitride nanotubes *Phys. Rev.* B **49** 5081–4
[7] Chopra N G, Luyken R J, Cherrey K, Crespi V H, Cohen M L, Louie S G and Zettl A 1995 Boron-Nitride Nanotubes *Science* **269** 966–7
[8] Kundalwal S I, Choyal V K, Luhadiya N and Choyal V 2020 Effect of carbon doping on electromechanical response of boron nitride nanosheets *Nanotechnology* **31** 405710
[9] Gupta M, Meguid S A and Kundalwal S I 2022 Synergistic effect of surface-flexoelectricity on electromechanical response of BN-based nanobeam *Int. J. Mech. Mater. Des.* **18** 3–19
[10] Du M, Bi J-Q, Wang W-L, Sun X-L and Long N-N 2011 Microstructure and properties of $SiO_2$ matrix reinforced by BN nanotubes and nanoparticles *J. Alloys Compd.* **509** 9996–10002
[11] Anjum N, Wang D, Gou F and Ke C 2024 Boron nitride nanotubes toughen silica ceramics *ACS Appl. Eng. Mater.* **2** 735–46
[12] Tank M, Leon A D, Huang W, Patadia M, Degraff J and Sweat R 2023 Manufacturing of stereolithographic 3D printed boron nitride nanotube-reinforced ceramic composites with improved thermal and mechanical performance *Funct. Compos. Struct.* **5** 015001
[13] Ashby M F and Cebon D 1993 Materials selection in mechanical design *J. Phys.* IV **03** C7–9
[14] Treacy M M J, Ebbesen T W and Gibson J M 1996 Exceptionally high Young's modulus observed for individual carbon nanotubes *Nature* **381** 678–80
[15] Chopra N G and Zettl A 1998 Measurement of the elastic modulus of a multi-wall boron nitride nanotube *Solid State Commun.* **105** 297–300
[16] Arenal R, Wang M-S, Xu Z, Loiseau A and Golberg D 2011 Young modulus, mechanical and electrical properties of isolated individual and bundled single-walled boron nitride nanotubes *Nanotechnology* **22** 265704
[17] Hernandez E, Goze C, Bernier P and Rubio A 1998 Elastic properties of C and BxCyNz composite nanotubes *Phys. Rev. Lett.* **80** 4502–5
[18] Choyal V, Choyal V K and Kundalwal S I 2019 Effect of atom vacancies on elastic and electronic properties of transversely isotropic boron nitride nanotubes: a comprehensive computational study *Comput. Mater. Sci.* **156** 332–45
[19] Suryavanshi A P, Yu M-F, Wen J, Tang C and Bando Y 2004 Elastic modulus and resonance behavior of boron nitride nanotubes *Appl. Phys. Lett.* **84** 2527–9
[20] Zhao Y, Chen X, Park C, Fay C C, Stupkiewicz S and Ke C 2014 Mechanical deformations of boron nitride nanotubes in crossed junctions *J. Appl. Phys.* **115** 164305
[21] Zheng M, Chen X, Park C, Fay C C, Pugno N M and Ke C 2013 Nanomechanical cutting of boron nitride nanotubes by atomic force microscopy *Nanotechnology* **24** 505719
[22] Wei X, Wang M-S, Bando Y and Golberg D 2010 Tensile tests on individual multi-walled boron nitride nanotubes *Adv. Mater.* **22** 4895–9
[23] Chen X, Dmuchowski C M, Park C, Fay C C and Ke C 2017 Quantitative characterization of structural and mechanical properties of boron nitride nanotubes in high temperature environments *Sci. Rep.* **7** 11388
[24] Tank M J, Reyes A N, Park J G, Scammell L R, Smith M W, De Leon A and Sweat R D 2022 Extreme thermal stability and dissociation mechanisms of purified boron nitride nanotubes: implications for high-temperature nanocomposites *ACS Appl. Nano Mater.* **5** 12444–53
[25] Zheng M, Chen X, Bae I-T, Ke C, Park C, Smith M W and Jordan K 2012 Radial mechanical properties of single-walled boron nitride nanotubes *Small* **8** 116–21
[26] Zheng M, Zou L-F, Wang H, Park C and Ke C 2012 Engineering radial deformations in single-walled carbon and boron nitride nanotubes using ultrathin nanomembranes *ACS Nano* **6** 1814–22
[27] Zheng M, Ke C, Bae I-T, Park C, Smith M W and Jordan K 2012 Radial elasticity of multi-walled boron nitride nanotubes *Nanotechnology* **23** 095703
[28] Zheng M, Zou L, Wang H, Park C and Ke C 2012 Quantifying the transverse deformability of double-walled carbon and boron nitride nanotubes using an ultrathin nanomembrane covering scheme *J. Appl. Phys.* **12** 104318
[29] Li N, Dmuchowski C M, Jiang Y, Yi C, Gou F, Deng J, Ke C and Chew H B 2022 Sliding energy landscape governs interfacial failure of nanotube-reinforced ceramic nanocomposites *Scr. Mater.* **210** 114413
[30] Yi C, Bagchi S, Gou F, Dmuchowski C M, Park C, Fay C C, Chew H B and Ke C 2019 Direct nanomechanical measurements of boron nitride nanotube—ceramic interfaces *Nanotechnology* **30** 025706
[31] Wang W-L, Bi J-Q, Wang S-R, Sun K-N, Du M, Long N-N and Bai Y-J 2011 Microstructure and mechanical properties of alumina ceramics reinforced by boron nitride nanotubes *J. Eur. Ceram. Soc.* **31** 2277–84

[32] Xu J-J, Bai Y-J, Wang W-L, Wang S-R, Han F-D, Qi Y-X and Bi J-Q 2012 Toughening and reinforcing zirconia ceramics by introducing boron nitride nanotubes *Mater. Sci. Eng.* A **546** 301–6
[33] Kothari R, Kundalwal S I and Sahu S K 2018 Transversely isotropic thermal properties of carbon nanotubes containing vacancies *Acta Mech.* **229** 2787–800
[34] Almeida C M R, Ghica M E and Durães L 2020 An overview on alumina-silica-based aerogels *Adv. Colloid Interface Sci.* **282** 102189
[35] De Sousa L L, Salomão R and Arantes V L 2017 Development and characterization of porous moldable refractory structures of the alumina-mullite-quartz system *Ceram. Int.* **43** 1362–70
[36] Jamaludin A R, Kasim S R, Abdullah M Z and Ahmad Z A 2016 Physical, mechanical, and thermal properties improvement of porous alumina substrate through dip-coating and re-sintering procedures *Ceram. Int.* **42** 7717–29
[37] Tallon C, Chuanuwatanakul C, Dunstan D E and Franks G V 2016 Mechanical strength and damage tolerance of highly porous alumina ceramics produced from sintered particle stabilized foams *Ceram. Int.* **42** 8478–87
[38] Wang L, An L, Zhao J, Shimai S, Mao X, Zhang J, Liu J and Wang S 2021 High-strength porous alumina ceramics prepared from stable wet foams *J. Adv. Ceram.* **10** 852–9
[39] Yang E, Jang E J, Lee J G, Yoon S, Lee J, Musselwhite N, Somorjai G A, Kwak J H and An K 2018 Acidic effect of porous alumina as supports for Pt nanoparticle catalysts in *n*-hexane reforming *Catal. Sci. Technol.* **8** 3295–303
[40] Takahashi T, Tanimoto R, Isobe T, Matsushita S and Nakajima A 2016 Surface modification of porous alumina filters for $CO_2$ separation using silane coupling agents *J. Membr. Sci.* **497** 216–20
[41] Wei Z, Li S, Li Y, Li X, Xiang R and Xu N 2018 Porous alumina ceramics with enhanced mechanical and thermal insulation properties based on sol-treated rice husk *Ceram. Int.* **44** 22616–21
[42] Liu J, Ren B, Zhu T, Yan S, Zhang X, Huo W, Chen Y and Yang J 2018 Enhanced mechanical properties and decreased thermal conductivity of porous alumina ceramics by optimizing pore structure *Ceram. Int.* **44** 13240–6
[43] Li Q, An X, Liang J, Liu Y, Hu K, Lu Z, Yue X, Li J, Zhou Y and Sun X 2022 Balancing flexural strength and porosity in DLP-3D printing $Al_2O_3$ cores for hollow turbine blades *J. Mater. Sci. Technol.* **104** 19–32
[44] Liu J, Li Q, Huo M, Zhang X, Yue X, Liang J and Li J 2022 Microstructure and mechanical properties of 3D-printed nano-silica reinforced alumina cores *Ceram. Int.* **48** 30282–93
[45] Zhang B, Gui X, Song P, Xu X, Guo L, Han Y, Wang L, Zhou C, Fan Y and Zhang X 2022 Three-dimensional printing of large-scale, high-resolution bioceramics with micronano inner porosity and customized surface characterization design for bone regeneration *ACS Appl. Mater. Interfaces* **14** 8804–15
[46] Qian C, Hu K, Shen Z, Wang Q, Li P and Lu Z 2023 Effect of sintering aids on mechanical properties and microstructure of alumina ceramic via stereolithography *Ceram. Int.* **49** 17506–23
[47] Smith M W, Jordan K C, Park C, Kim J-W, Lillehei P T, Crooks R and Harrison J S 2009 Very long single- and few-walled boron nitride nanotubes via the pressurized vapor/condenser method *Nanotechnology* **20** 505604
[48] Yamakov V, Park C, Kang J H, Chen X, Ke C and Fay C 2017 Piezoelectric and elastic properties of multiwall boron-nitride nanotubes and their fibers: a molecular dynamics study *Comput. Mater. Sci.* **135** 29–42
[49] Chen S, Wang C-S, Zheng W, Wu J-M, Yan C-Z and Shi Y-S 2022 Effects of particle size distribution and sintering temperature on properties of alumina mold material prepared by stereolithography *Ceram. Int.* **48** 6069–77
[50] Huang W, Wu Y, Chen W, Chen H, He J, Yan J, Chen C, Song Y, Ji H and Xu H 2022 Reinforcement effect in printing precision and sintering performance for liquid crystal display stereolithography additive manufacturing of alumina ceramics *Ceram. Int.* **48** 33809–18
[51] Meir S, Kalabukhov S, Frage N and Hayun S 2015 Mechanical properties of $Al_2O_3\backslash$Ti composites fabricated by spark plasma sintering *Ceram. Int.* **41** 4637–43
[52] Anjum N, Alsmairat O Q, Liu Z, Park C, Fay C C and Ke C 2022 Mechanical characterization of electrospun boron nitride nanotube-reinforced polymer nanocomposite microfibers *J. Mater. Res.* **37** 4594–604
[53] Kuscer D, Bantan I, Hrovat M and Malič B 2017 The microstructure, coefficient of thermal expansion and flexural strength of cordierite ceramics prepared from alumina with different particle sizes *J. Eur. Ceram. Soc.* **37** 739–46
[54] Turner P S 1942 The problem of thermal-expansion stresses in reinforced plastics. *Natl. Advis. Comm. Aeronaut. NACA Wartime Rep*
[55] Shirasu K, Nakamura A, Yamamoto G, Ogasawara T, Shimamura Y, Inoue Y and Hashida T 2017 Potential use of CNTs for production of zero thermal expansion coefficient composite materials: an experimental evaluation of axial thermal expansion coefficient of CNTs using a combination of thermal expansion and uniaxial tensile tests *Composites A.* **95** 152–60
[56] Latella B A and Liu T 2005 High-temperature young's modulus of alumina during sintering *J. Am. Ceram. Soc.* **88** 773–6
[57] Han T, Luo Y and Wang C 2013 Effects of temperature and strain rate on the mechanical properties of hexagonal boron nitride nanosheets *J. Phys. Appl. Phys.* **47** 025303
[58] Chang H, Lu M, Arias-Monje P J, Luo J, Park C and Kumar S 2019 Determining the orientation and interfacial stress transfer of boron nitride nanotube composite fibers for reinforced polymeric materials *ACS Appl. Nano Mater.* **2** 6670–6
[59] Wang W, Li Z, Prestat E, Hashimoto T, Guan J, Kim K S, Kingston C T, Simard B and Young R J 2020 Reinforcement of polymer-based nanocomposites by thermally conductive and electrically insulating boron nitride nanotubes *ACS Appl. Nano Mater.* **3** 364–74
[60] Alsmairat O Q, Gou F, Dmuchowski C M, Chiarot P R, Park C, Miles R N and Ke C 2020 Quantifying the interfacial load transfer in electrospun carbon nanotube polymer nanocomposite microfibers by using *in situ* Raman micromechanical characterization techniques *J. Phys. D: Appl. Phys.* **53** 365302
[61] Jiang Y, Li N, Liu Z, Yi C, Zhou H, Park C, Fay C C, Deng J, Chew H B and Ke C 2023 Exceptionally strong boron nitride nanotube aluminum composite interfaces *Extrem. Mech. Lett.* **59** 101952